Supplementary figures and table for

Structural and functional insights into KIDINS220-mediated regulation of the phosphate exporter XPR1

Yan Liu[1,#], Jie Zhang[1,#], Lihuan Jiang[1,#], Kun Li[1], Kangning Tan[1], Haitao He[1], Zhangmeng Du[1], Jiaqi Zuo[1], Shuo Cao[1], Xuemei Peng[1], Guojing Bu[1], Wenhui Zhang[1], Yanke Chen[1], Yong Wang[2], Zhu Liu[1*]

[1]National Key Laboratory of Crop Genetic Improvement, Hubei Provincial Research Center for Basic Biological Sciences, Hubei Hongshan Laboratory, Huazhong Agricultural University, Wuhan 430070, China.

[2]College of Life Sciences, Zhejiang University, Hangzhou, China

[s#]These authors contributed equally to this work.

[*]Corresponding author: liuzhu@mail.hzau.edu.cn (Z. L.)

This file includes:

Supplementary Figs. 1-15

Supplementary Tables 1

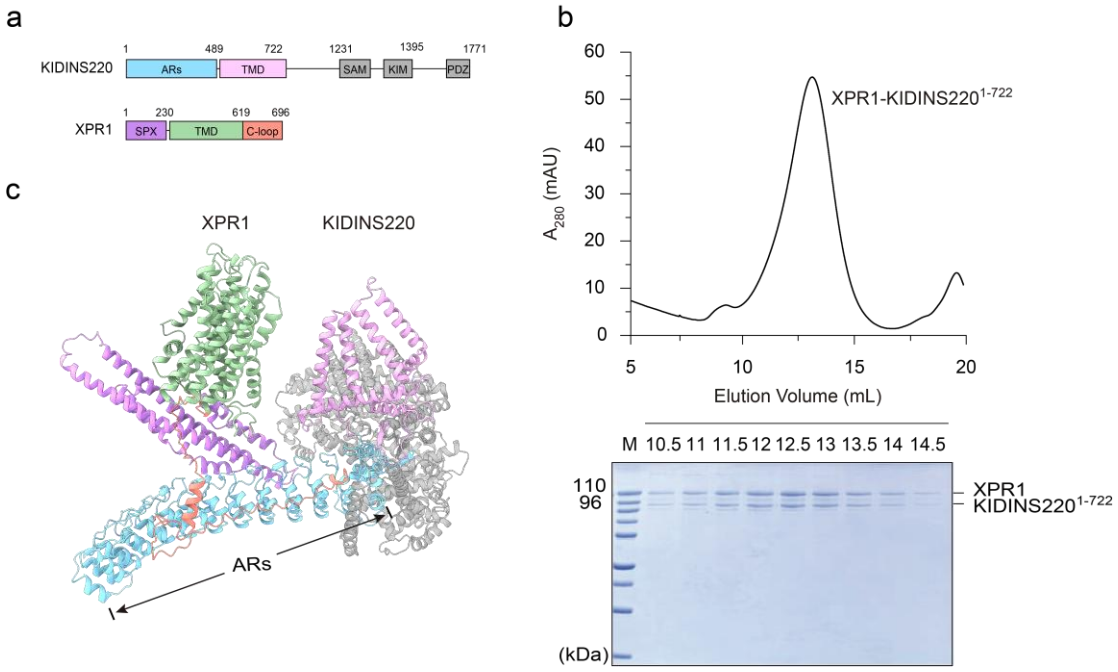

Supplementary Fig. 1. Representative size-exclusion chromatography (SEC) purification and structural prediction of XPR1–KIDINS220$^{1-722}$ complex. a, Schematic domain organization of XPR1 and KIDINS220. In KIDINS220, the N-terminal ankyrin-repeats (ARs) domain is shown in cyan, the four-helix transmembrane domain (TMD) in pink, and the C-terminal region in gray, including the cytosolic sterile alpha motif (SAM), kinase interaction motif (KIM), and PDZ domain. In XPR1, the SPX domain is shown in purple, the transmembrane domain (TMD) in green, and the C-loop in salmon. **b,** Fractions from size-exclusion chromatography (SEC) were resolved by 12% SDS-PAGE, and the peak fractions were collected and concentrated for further use. **c,** AlphaFold3-predicted structure of the XPR1–KIDINS220 complex. The domains are colored consistently with the scheme shown in panel (**a**). This predicted model shows that KIDINS220 interacts with the C-terminus of XPR1, surrounding the SPX domain. Full-length proteins were used for prediction. The model shown represents the highest-scoring prediction, with an ipTM confidence score of 0.43.

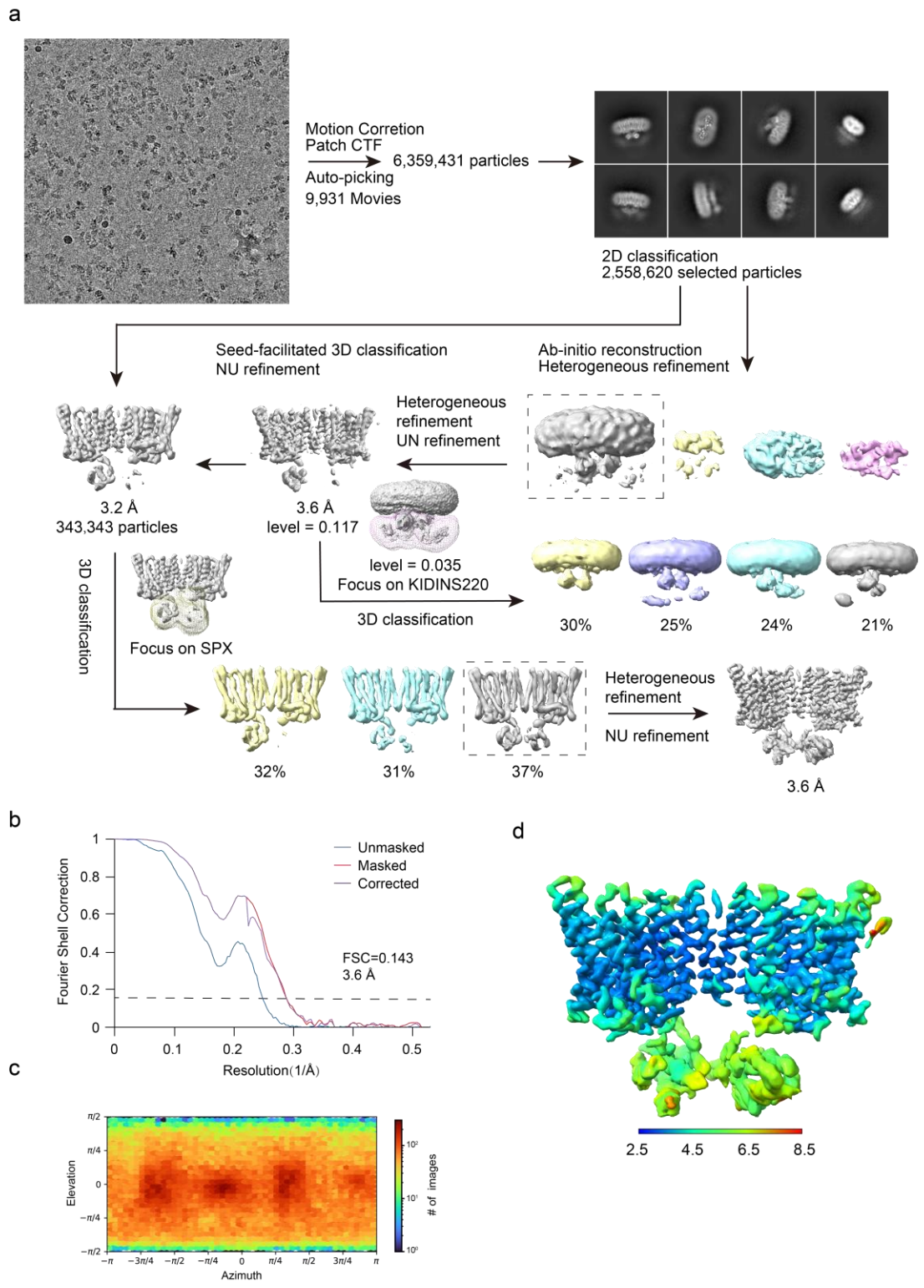

Supplementary Fig. 2. Cryo-EM data processing workflow of XPR1-KIDINS220$^{1-722}$ in the presence of 1 mM $InsP_6$ ($XPR1^{InsP6}$). a, Flowchart summarizing the EM data processing. The 3D refinement generated a 3.6 Å map. **b,** Gold-standard Fourier shell

correlation (FSC) curves for the final map refinement. **c,** Angular distribution of the particles used for reconstruction. **d,** Local resolution from 3D refinement for the final reconstructions.

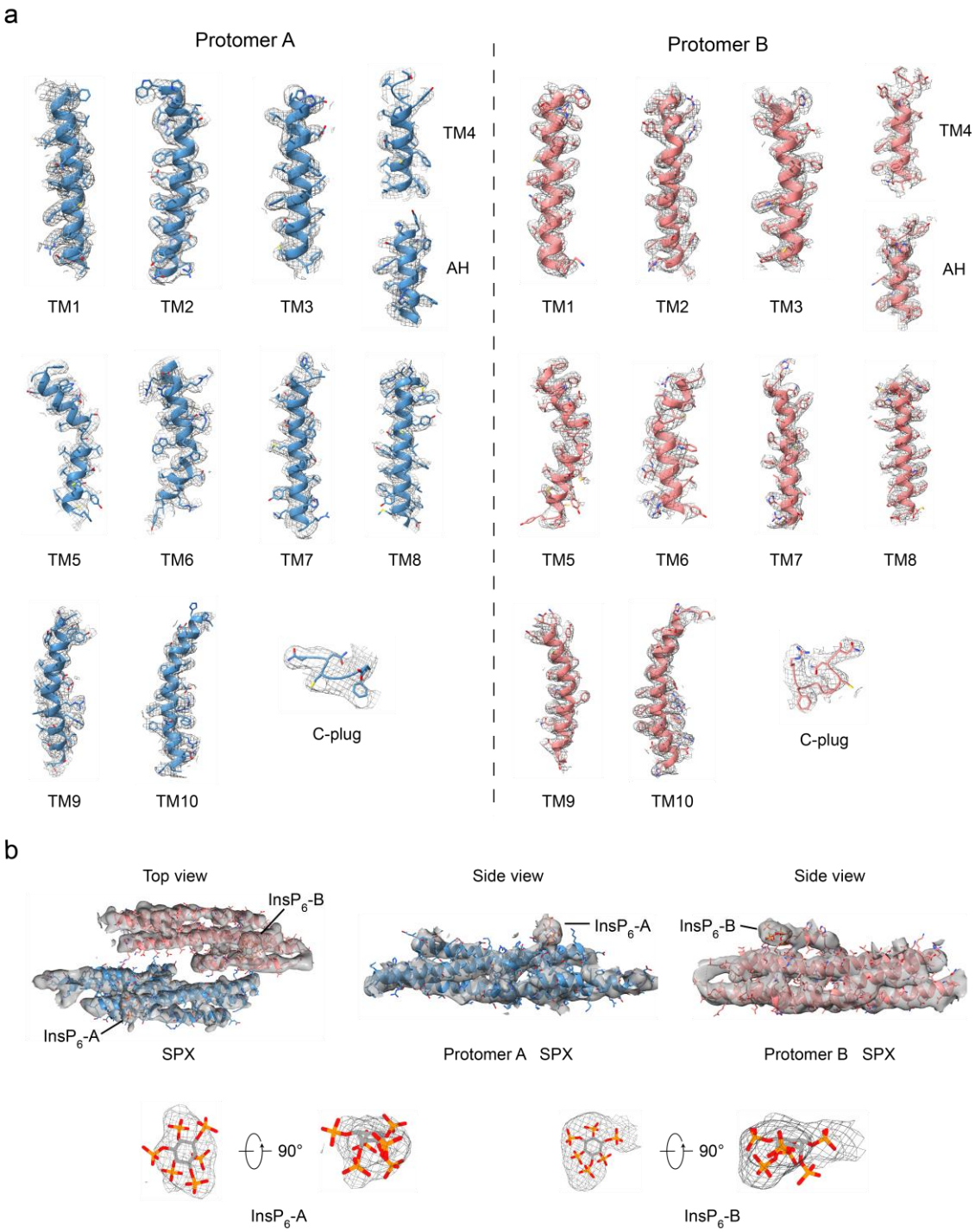

Supplementary Fig. 3. Cryo-EM densities of KIDINS220$^{1-722}$-associated XPR1^{InsP6} structural elements. a, Cryo-EM densities corresponding to individual transmembrane

helices (TM1–TM10), the amphipathic helix (AH), and the C-plug from protomer A (blue) and protomer B (light coral). Map contour level = 0.064 in ChimeraX. **b,** Cryo-EM densities of the SPX domains and the bound $InsP_6$ molecules, shown from top and side views for protomers A and B. Map contour level = 0.0.068 in ChimeraX. The densities of the individual $InsP_6$ molecules are shown separately as gray meshes and contoured at a level of 0.18 in ChimeraX.

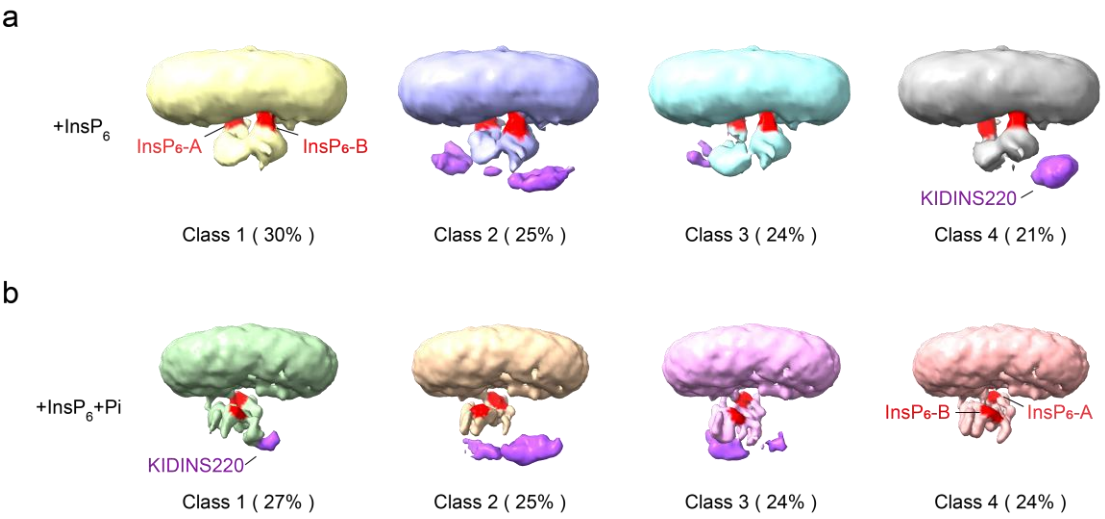

Supplementary Fig. 4. Dynamic densities of KIDINS220$^{1-722}$ revealed by cryo-EM analysis. a-b, Representative 3D classes of the XPR1–KIDINS220$^{1-722}$ complex reconstructed in the presence of (**a**) $InsP_6$, and (**b**) $InsP_6$ plus phosphate. Four distinct classes were resolved per condition, with particle proportions indicated (parentheses). $InsP_6$ molecules ($InsP_6$-A/B) bound to SPX domains are shown in red. The densities attributed to KIDINS220 are shown in purple. Three-dimensional classification was performed based on features of the KIDINS220 density. Its density exhibits variable positioning and occupancy across classes, reflecting conformational dynamics of the regulatory complex.

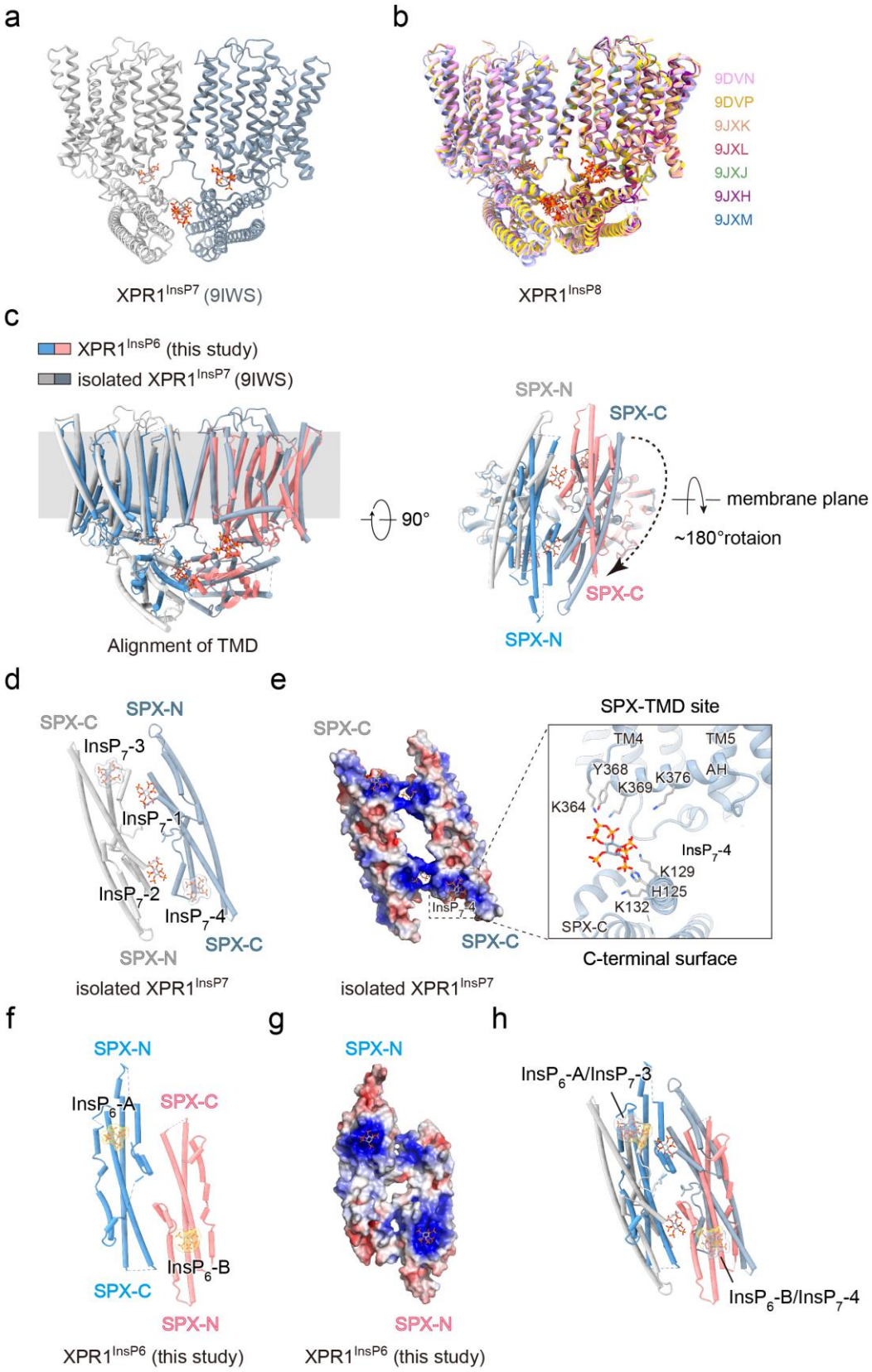

Supplementary Fig. 5. Comparison of SPX conformations and inositol phosphate–binding interfaces in inositol phosphate–bound XPR1 structures. a, Cryo–EM

structure of XPR1 bound to $InsP_7$ (PDB: 9IWS). One protomer is colored in gray and the other in slate blue. **b,** $InsP_8$-bound XPR1 structures (PDB: 9DVN, 9DVP, 9JXK, 9JXL, 9JXJ, 9JXH, and 9JXM). **c,** Structural comparison between $KIDINS220^{1-722}$-associated $XPR1^{InsP6}$ (this study) and isolated $XPR1^{InsP7}$ (9IWS) based on TMD-based structural alignment. Alignment of the transmembrane domains reveals an ~180° reorientation of the SPX domain relative to the membrane plane. **d,** SPX conformations and $InsP_7$-binding positions in isolated $XPR1^{InsP7}$ (9IWS). Distinct $InsP_7$ molecules are labeled as $InsP_7$-1 to $InsP_7$-4. **e,** Electrostatic surface representation of isolated $XPR1^{InsP7}$ showing the $InsP_7$-interacting surface, same projection as in (**d**). Inset highlights the $InsP_7$-4 binding site on the C-terminal surface of the SPX domain, which is formed together with the amphipathic helix (AH) within the TMD. **f,** SPX conformations and $InsP_6$-binding positions in $KIDINS220^{1-722}$-associated $XPR1^{InsP6}$ (this study). Bound $InsP_6$ molecules are labeled as $InsP_6$-A and $InsP_6$-B. **g**, Electrostatic surface representation of $KIDINS220^{1-722}$-associated $XPR1^{InsP6}$ showing the $InsP_6$-binding pocket, same projection as in (**f**). **h**, Structural comparison of inositol phosphate positions between $KIDINS220^{1-722}$-associated $XPR1^{InsP6}$ and isolated $XPR1^{InsP7}$.

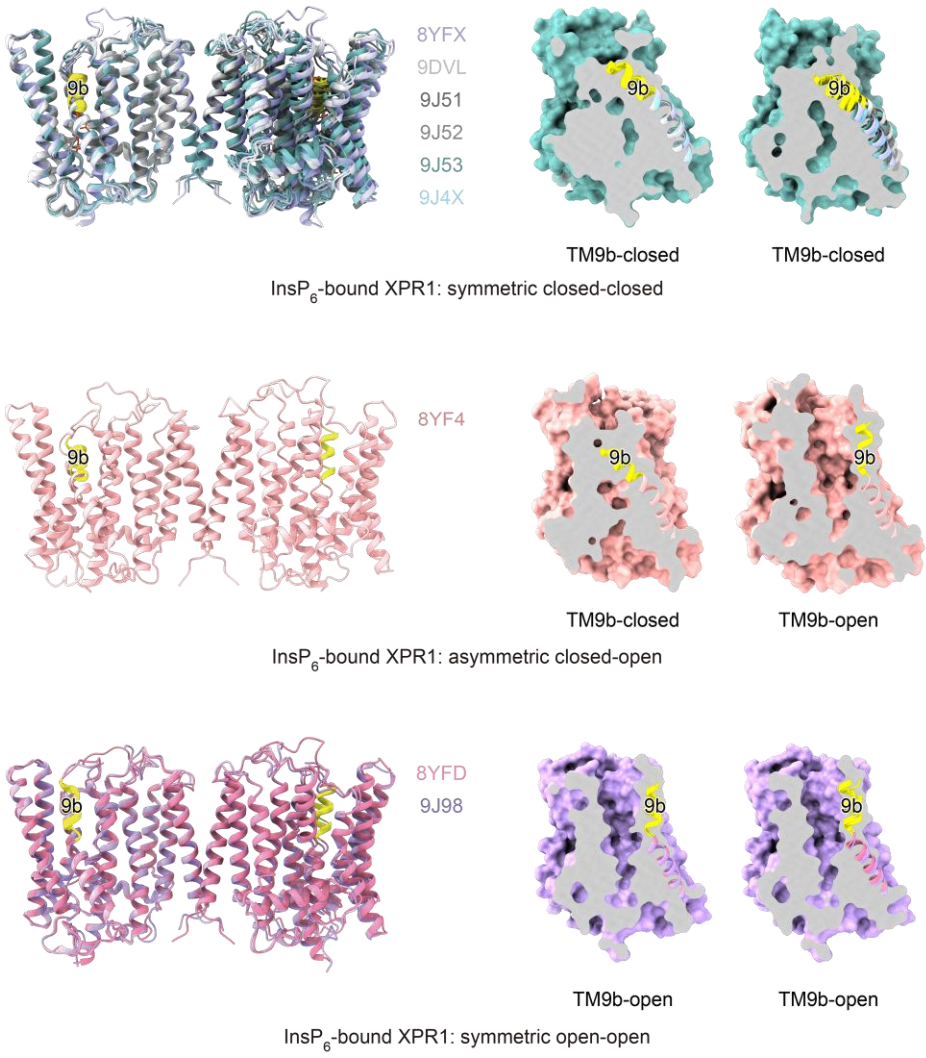

Supplementary Fig. 6. Conformational landscape of $InsP_6$-bound XPR1. (Top) Structural comparison of $InsP_6$-bound XPR1 in symmetric closed states. Left: Overlay of the XPR1 structures in the presence of $InsP_6$ (PDB: 8YFX, 9DVL, 9J51, 9J52, 9J53, and 9J4X) showing the symmetric closed-conformation of TM9b (yellow). Right: Surface representation of the TM9b-closed state in XPR1. (Middle) Structural comparison of $InsP_6$-bound XPR1 in asymmetric closed-open states. Left: Overlay of the XPR1 structure in the presence of $InsP_6$ (PDB: 8YF4) showing the asymmetric closed-open conformation of TM9b. Right: Surface representation of the TM9b-closed and TM9b-open states in XPR1. (Bottom) Structural comparison of $InsP_6$-bound XPR1 in symmetric open-open states. Left: Overlay of the XPR1 structure in the presence of

$InsP_6$ (PDB: 8YFD and 9J98) showing the symmetric open-conformation of TM9b. Right: Surface representation of the TM9b-open state in XPR1.

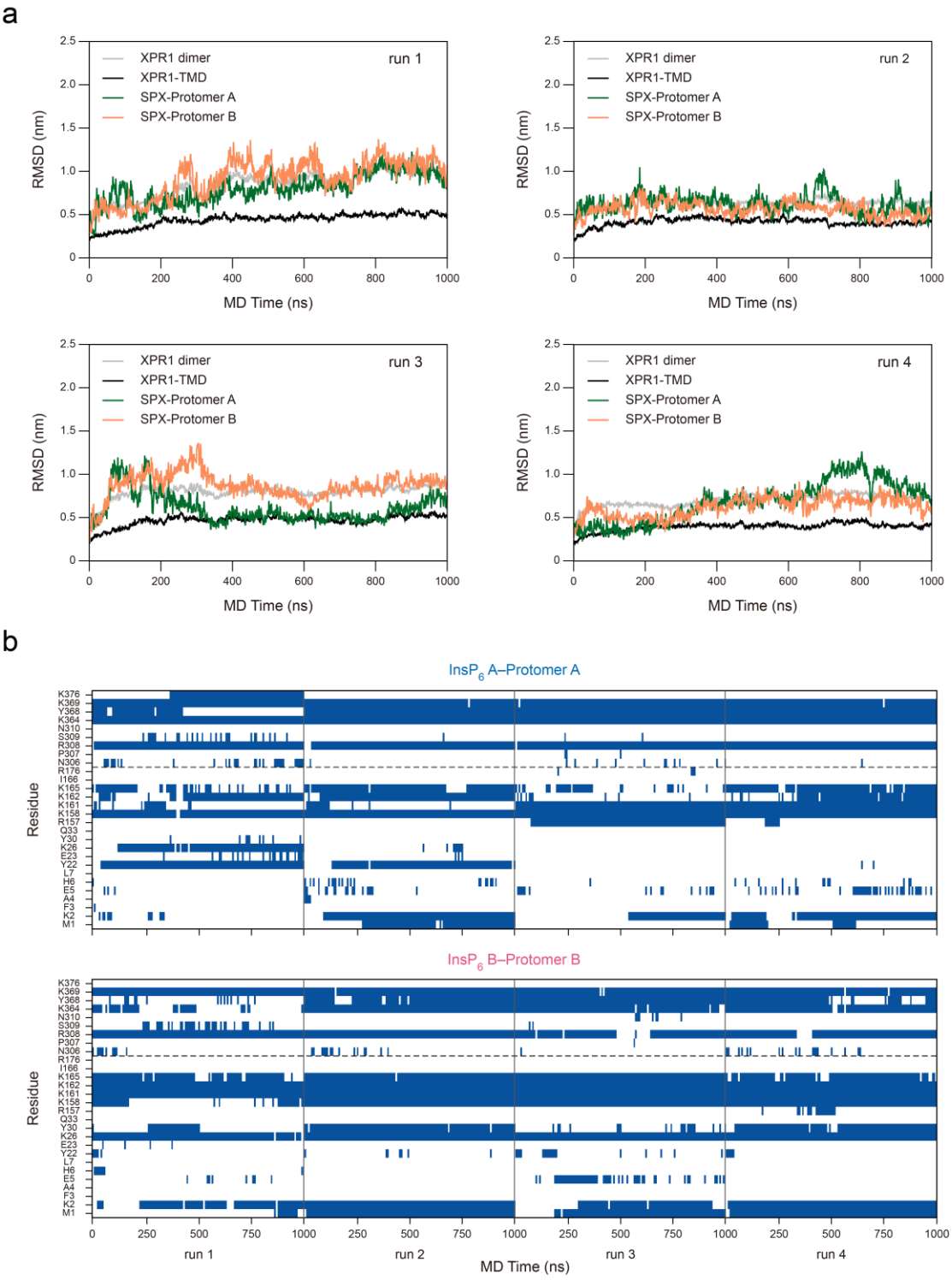

Supplementary Fig. 7. Molecular dynamics stability and ligand-residue contact analysis of XPR1 complexes across four independent 1 μs MD simulations of

XPR1^{InsP6} in the KIDINS220$^{1-722}$-bound conformation. a, RMSD trajectories over 1 µs MD trajectories for four replicate runs (run 1–4). RMSD values are shown for the full XPR1 dimer (light grey), XPR1-TMD (black), and the SPX domains of protomers A (green) and B (orange). **b,** Contact occupancy heatmaps tracking persistent atomic contacts between $InsP_6$ and individual residues of Protomer A (top) and Protomer B (bottom) across the four 1 µs replicates. Vertical axis labels denote XPR1 residue identifiers; horizontal axis is simulation time (ns), partitioned by replicate run. Solid blue bars indicate time windows where $InsP_6$-residue interactions are maintained. Dashed lines are used to separate TMD and SPX domain residues.

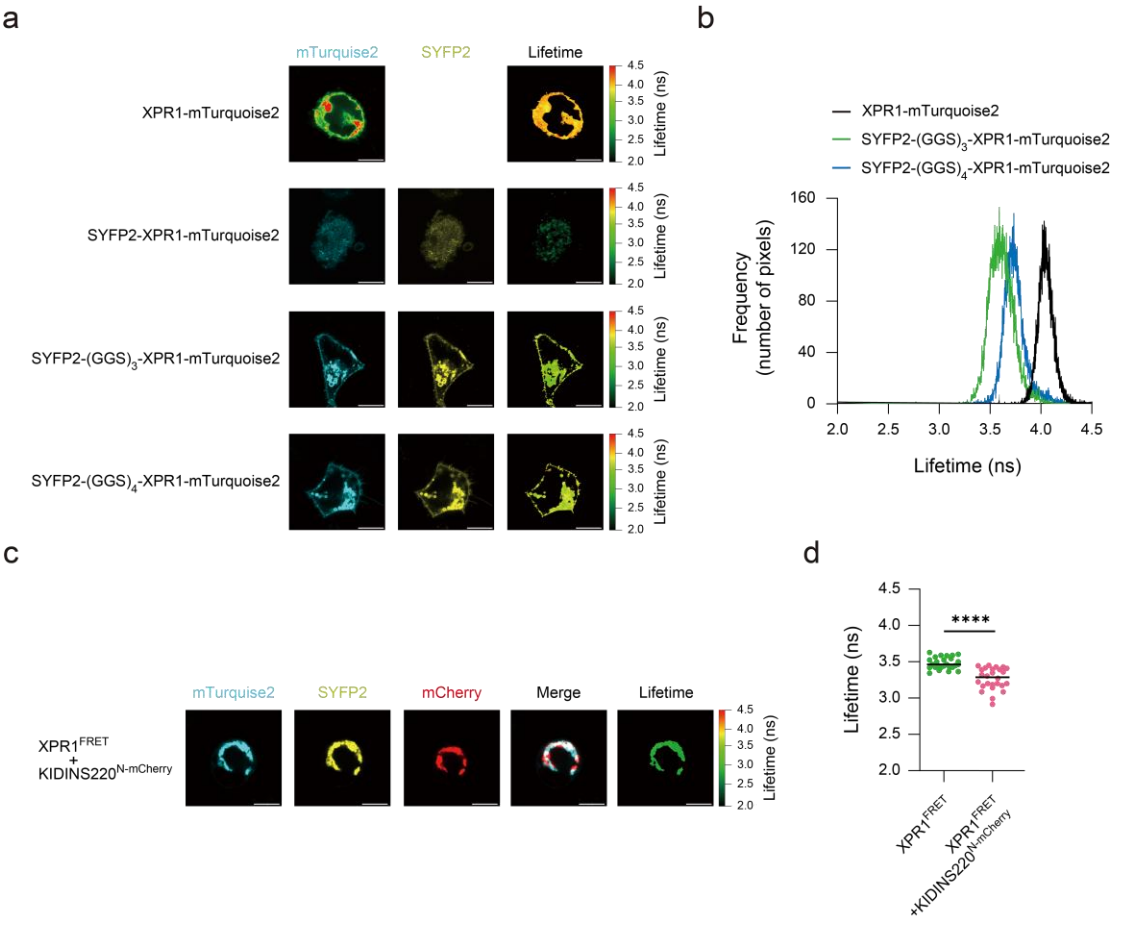

Supplementary Fig. 8. Optimization and validation of XPR1 FRET sensors for detecting KIDINS220-induced conformational changes. a, FLIM characterization of XPR1 FRET sensor variants. Representative images showing mTurquoise2 donor

lifetimes (τ_D) for: Donor control: XPR1-mTurquoise2 ($XPR1^{Donor}$); Direct fusion: SYFP2-XPR1-mTurquoise2 (no linker); Optimized FRET sensor: SYFP2-$(GGS)_3$-XPR1-mTurquoise2 and extended linker SYFP2-$(GGS)_4$-XPR1-mTurquoise2 ($XPR1^{FRET}$). Pseudocolor scale: 2.0-4.5 ns. Scale bars, 10 μm. **b,** Representative lifetime distribution histograms corresponding to (**a**). **c,** Orthogonal validation using N-terminally tagged KIDINS220. FLIM images of $XPR1^{FRET}$ co-expressed with mCherry-KIDINS220 confirm τ_D reduction. **d,** Quantification of mTurquoise2 fluorescence lifetime. n ⩾ 25 cells per group. Dots represent individual cells, and horizontal lines indicate the mean. ****p < 0.0001 (unpaired two-tailed Welch's t-test).

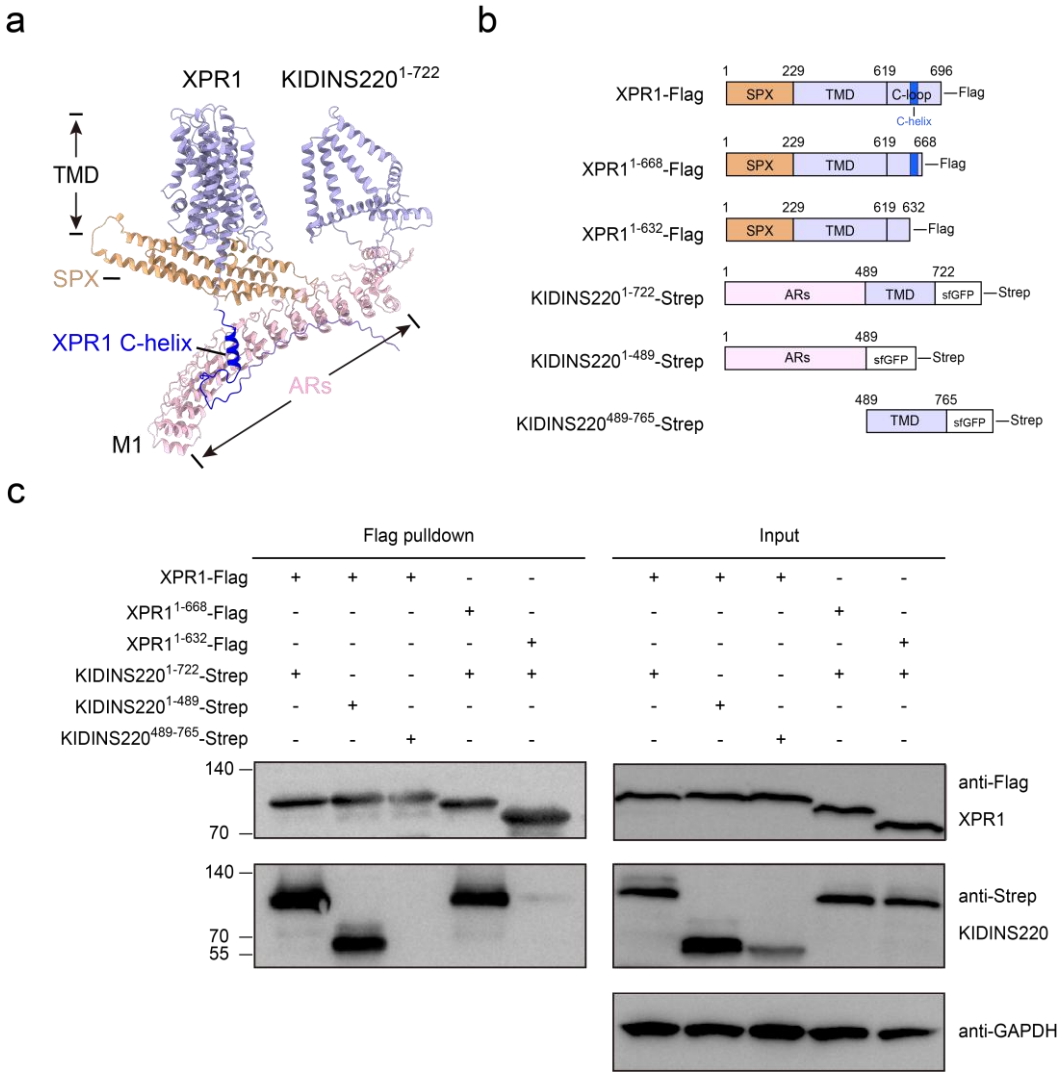

Supplementary Fig. 9. Structural and biochemical mapping of the XPR1–KIDINS220 interface. a, AlphaFold3-predicted structure of the XPR1–$KIDINS220^{1-}$

^{722} complex (ipTM = 0.54). The C-terminal α-helix of XPR1 (residues 633-668, blue) is predicted to dock into the N-terminal armadillo repeat (AR) groove of truncated KIDINS220 (1-722) (pink). A close-up view of the predicted interface is depicted in the main figure 2c. **b,** Domain schematics and constructs used for co-expression and interaction assays. Truncations of XPR1 or KIDINS220 were designed to evaluate the minimal regions required for complex formation. **c,** Domain-specific binding requirements demonstrated by co-immunoprecipitation. Anti-Flag pulldowns of XPR1 constructs co-expressed with Strep-tagged KIDINS220 variants. Input controls verify expression (right). GAPDH was used as a loading control to indicate comparable cell input. Blots representative of n=3 independent experiments.

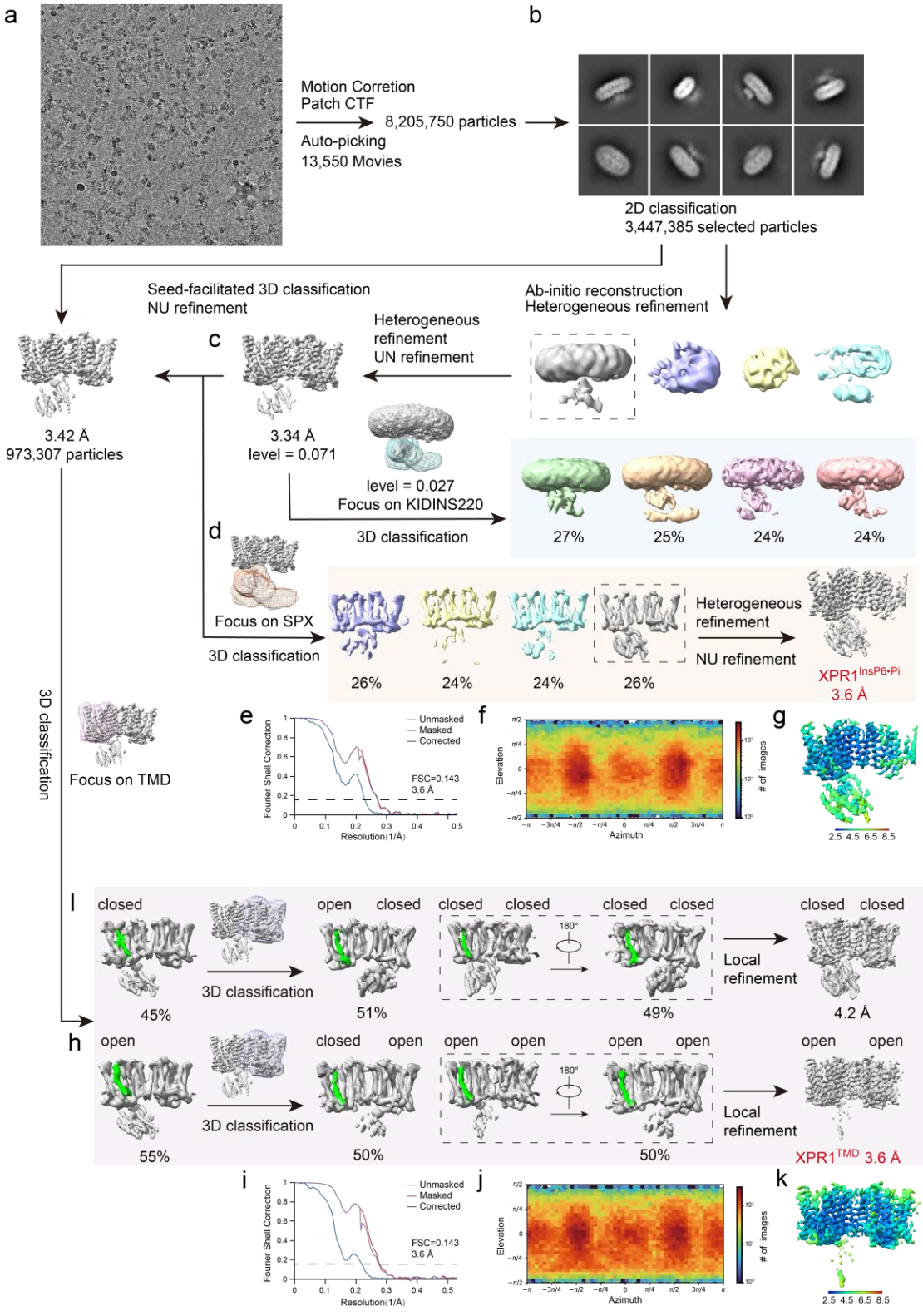

Supplementary Fig. 10. Cryo-EM data processing workflow of XPR1-KIDINS220$^{1-722}$ in the presence of 1 mM InsP6 and 25 mM phosphate (XPR1$^{InsP6•Pi}$

/XPR1^{TMD}). a-d, Flow chart for EM data processing. The 3D refinement generated a 3.6 Å map, designated XPR1$^{InsP6•Pi}$. **e-g,** Gold-standard Fourier shell correlation (FSC) curves, angular distribution plots, and local resolution from 3D refinement for the XPR1$^{InsP6•Pi}$ map reconstruction. **h,** Focus refinement on TMD generated a 3.6 Å map, designated XPR1^{TMD}. **i-k,** Gold-standard Fourier shell correlation (FSC) curves, angular distribution plot, and local resolution from 3D refinement for the XPR1^{TMD} map reconstruction. **l,** Focus refinement on TMD resolve TMD conformational heterogeneity.

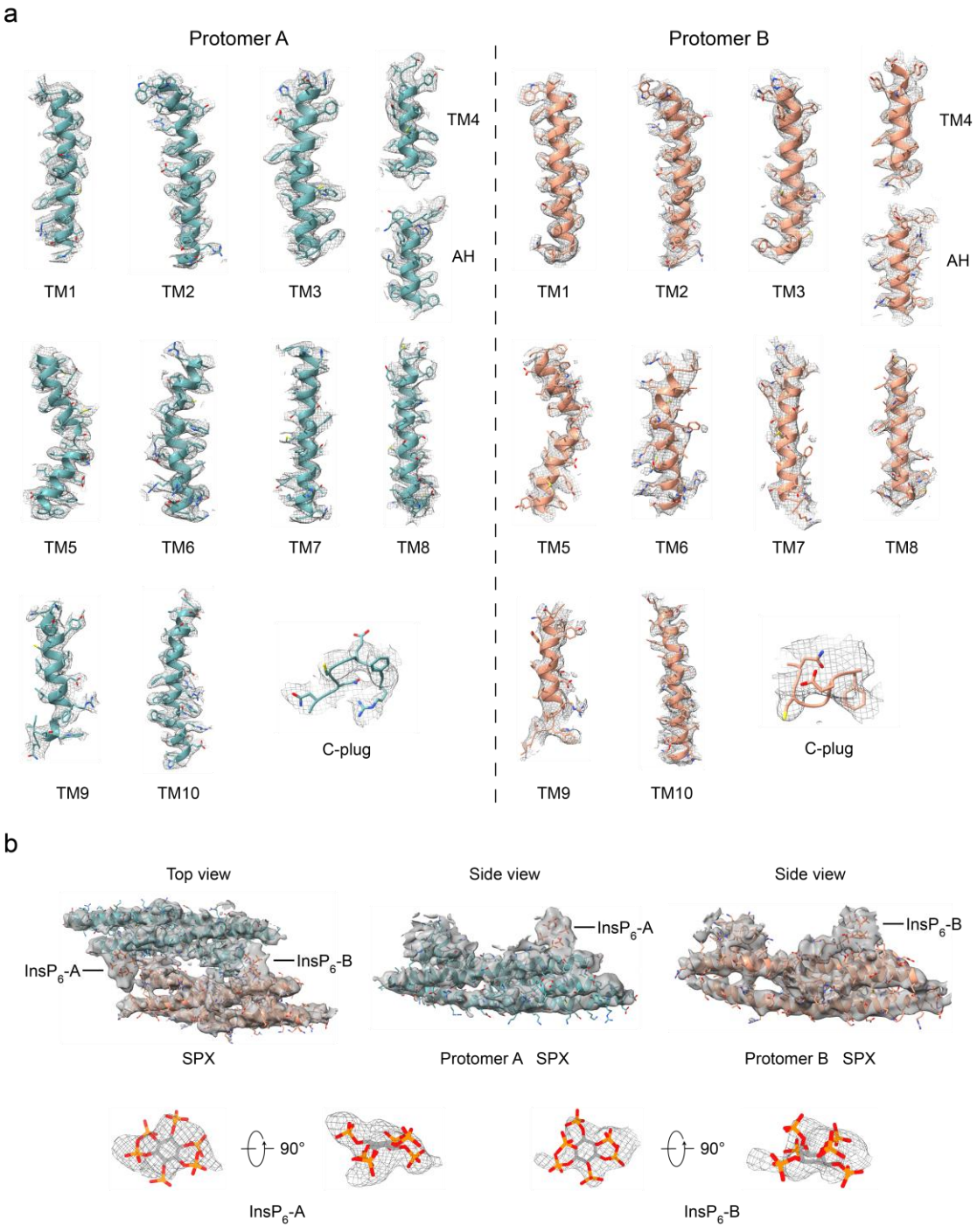

145

146 **Supplementary Fig. 11. Cryo-EM densities of KIDINS220$^{1-722}$-associated**
147 **XPR1$^{InsP6•Pi}$ structural elements. a,** Cryo-EM densities corresponding to individual
148 transmembrane helices (TM1–TM10), the amphipathic helix (AH), and the C-plug
149 from protomer A (teal) and protomer B (salmon). Map contour level = 0.061 in
150 ChimeraX. **b,** Cryo-EM densities of the SPX domains and the bound $InsP_6$ molecules,

shown from top and side views for protomers A and B. Map contour level = 0.063 in ChimeraX. The densities of the individual $InsP_6$ molecules are shown separately as gray meshes, with $InsP_6$-A and $InsP_6$-B displayed at contour levels of 0.113 and 0.15, respectively, in ChimeraX.

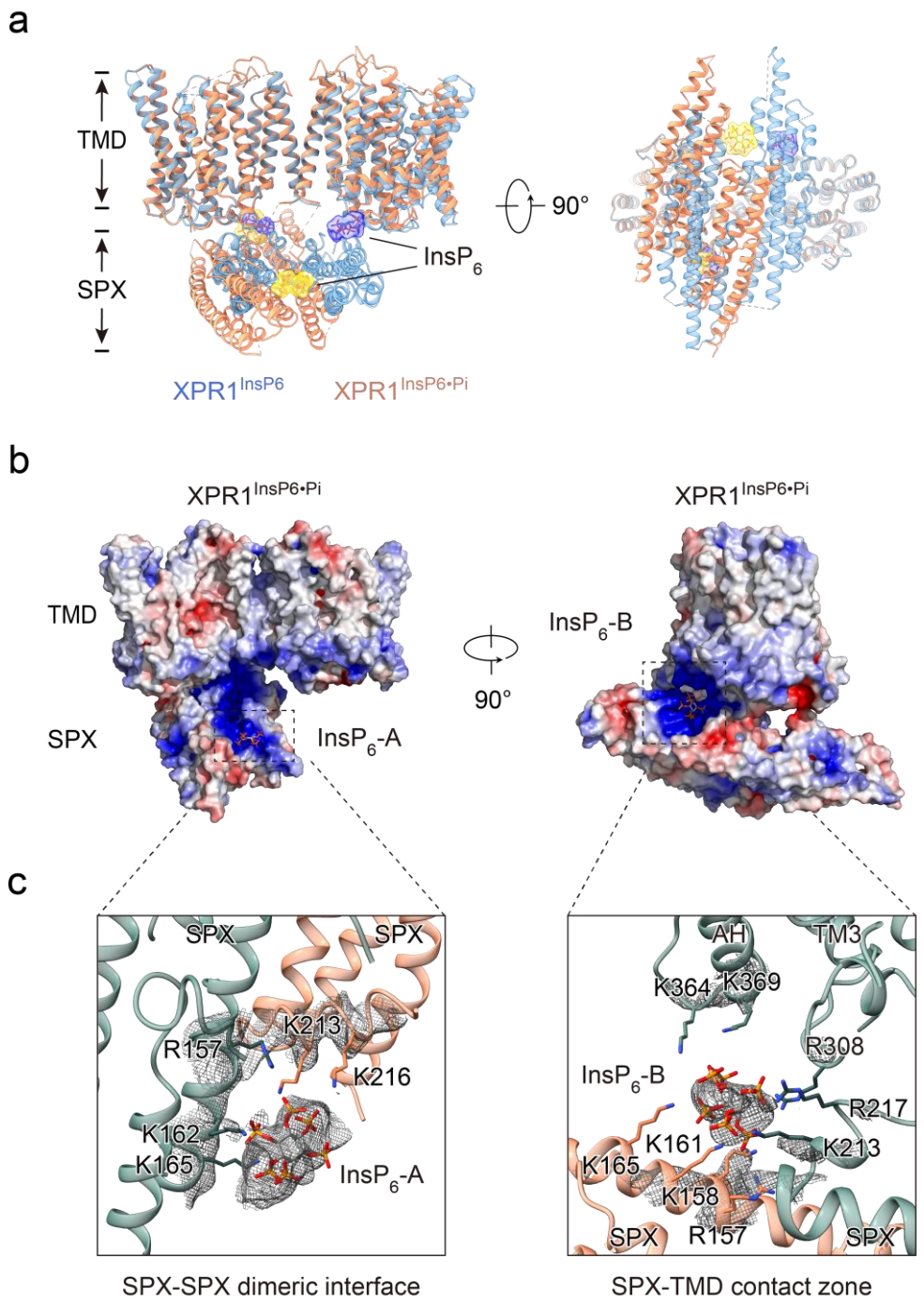

Supplementary Fig. 12. Structural comparison between KIDINS220$^{1-722}$-associated XPR1$^{InsP6•Pi}$ and the XPR1^{InsP6}. a, Structural comparison between

XPR1^{InsP6} and XPR1$^{InsP6•Pi}$ showing lateral deflection of the SPX domain toward one side of the TMD dimer and its repositioning beneath the membrane plane. **b,** Electrostatic surface representations of XPR1$^{InsP6•Pi}$ showing two electropositive interfacial clefts generated by SPX repositioning. Putative $InsP_6$ molecules are positioned within the SPX–SPX dimeric interface and the SPX–TMD contact zone. **c,** Zoomed-in views of the interfacial regions. The densities corresponding to $InsP_6$-A surface and $InsP_6$-B surface are displayed at contour levels of 0.076 and 0.169, respectively.

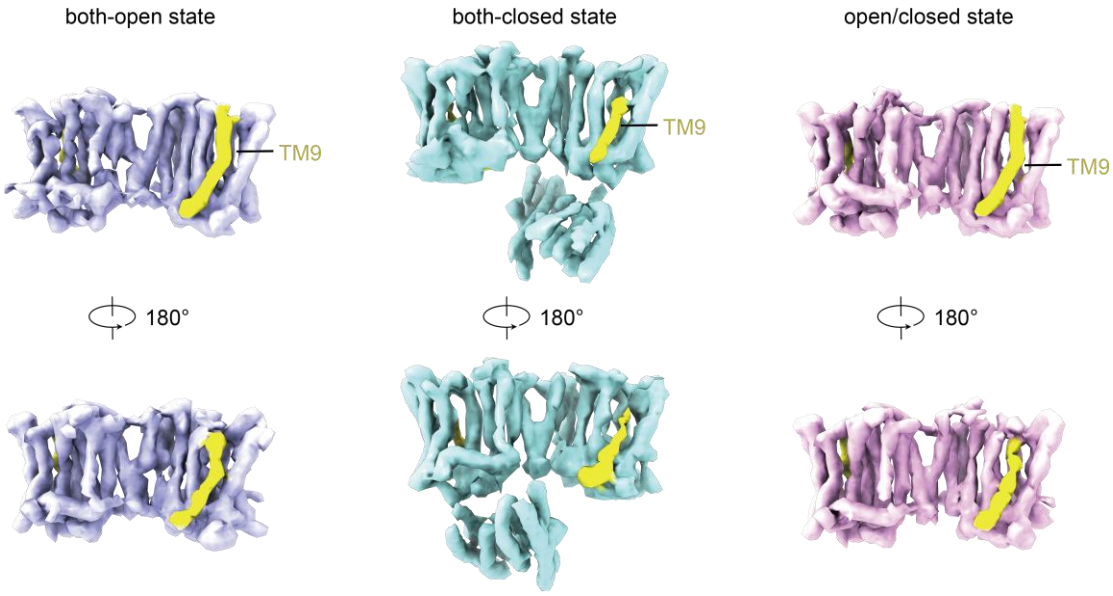

Supplementary Fig. 13. Diversity of TM9 gate conformations and subunit-wise independence. 3D variability and local-resolution analyses of the KIDINS220-associated XPR1 in the presence of $InsP_6$ and phosphate revealed that the dimer samples three recurrent TM9b configurations: a both-open state (left), a both-closed state (middle), and an asymmetric open/closed state (right). The cryo-EM maps are shown at two opposite orientations, with TM9 helices highlighted in yellow.

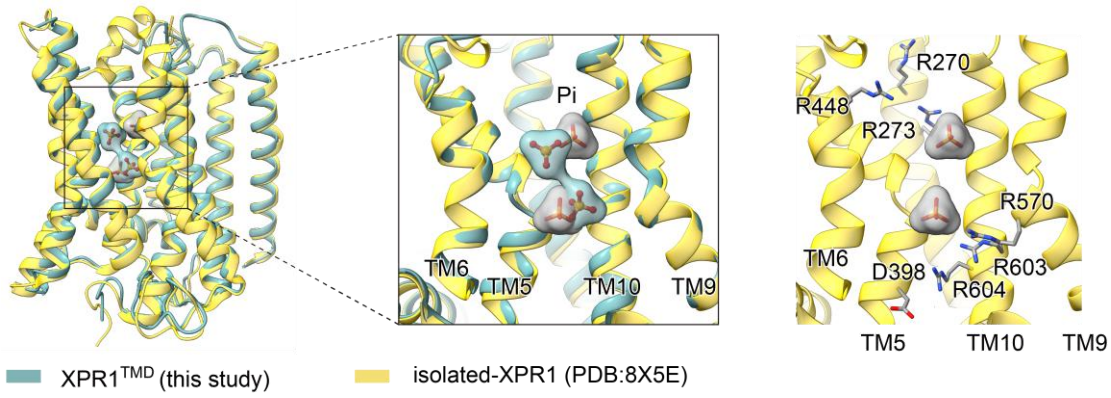

Supplementary Fig. 14. Structural comparison of phosphate positions in KIDINS220$^{1-722}$-associated XPR1^{TMD} and isolated-XPR1. Left, superposition of XPR1^{TMD} from this study (teal) and isolated-XPR1 (PDB: 8X5E, yellow). Middle, enlarged view of the superposed transmembrane phosphate-binding region in the two structures, showing the relative positions of the two phosphate ions (Pi). The phosphate ions in XPR1^{TMD} from this study are shown as teal surfaces, whereas the phosphate ion in isolated-XPR1 (PDB: 8X5E) is shown as a gray surface. Right, close-up view of the corresponding phosphate-binding region in isolated-XPR1, showing the residues surrounding the cavity.

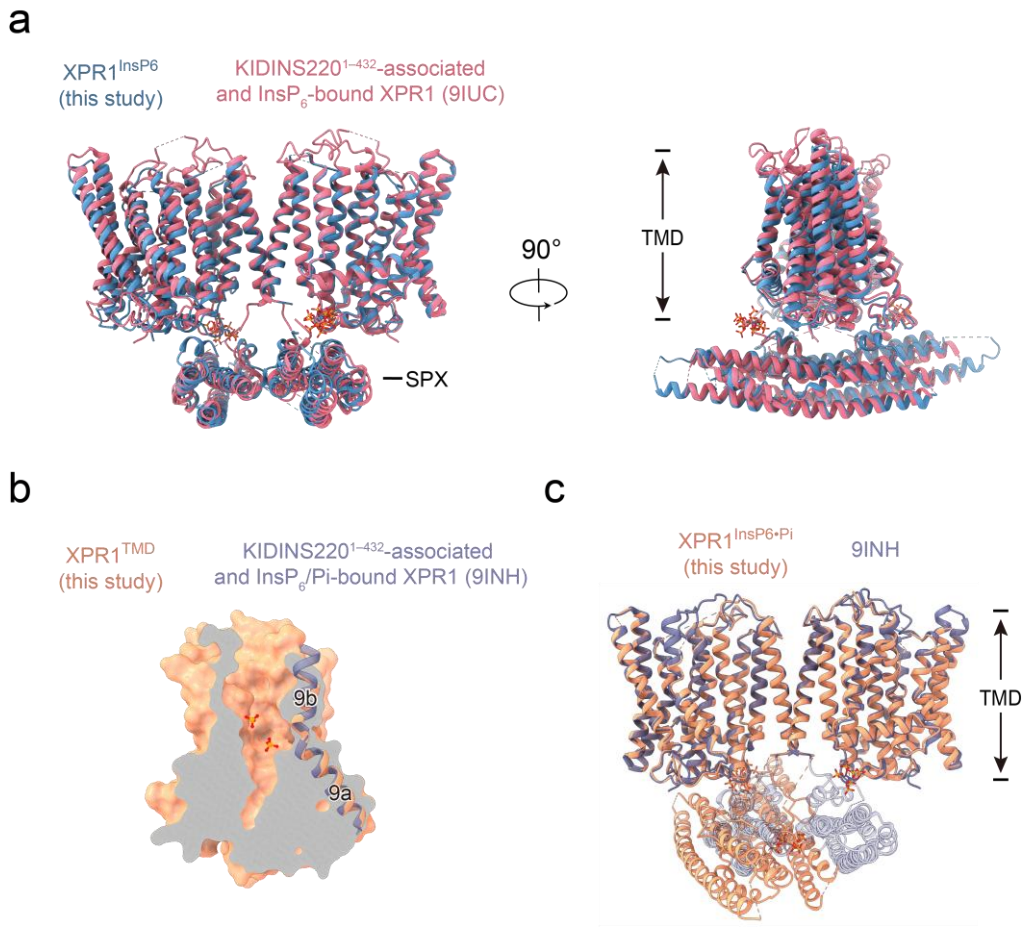

Supplementary Fig. 15. Comparison of our KIDINS220-associated XPR1 structures and reported relevant structures. a, Superimposition of the present $XPR1^{InsP6}$ structure (blue) with the reported $KIDINS220^{1–432}$-associated and $InsP_6$-bound XPR1 structure (pink; PDB: 9IUC) reveals similar overall architecture. **b,** TMD surface representation comparing the present Pi-bound XPR1 structure (orange; $XPR1^{TMD}$) with the $KIDINS220^{1–432}$-associated and $InsP_6$/Pi-bound XPR1 structure (purple; PDB: 9INH). The TM9 gate helix is indicated, with both structures adopting a TM9b-open conformation. **c,** Overlay of the present $XPR1^{InsP6•Pi}$ structure (orange) with the $KIDINS220^{1–432}$-associated and $InsP_6$/Pi-bound XPR1 structure (purple; PDB: 9INH). The two structures adopt different SPX orientations.

196 **Supplementary Table 1.** Cryo-EM data collection and refinement statistics.

	$XPR1^{InsP6}$ PDB: 22ZK EMDB: EMD-68791	$XPR1^{InsP6•Pi}$ PDB: 22ZH EMDB: EMD-68789	$XPR1^{TMD}$ PDB: 22ZI EMDB: EMD-68790
Data collection and processing			
Microscope	Krios G4	Krios G4	
Voltage (kV)	300	300	
Camera	Falcon 4	Falcon 4	
Magnification	130,000	165,000	
Pixel size at detector (Å/pixel)	0.93	0.73	
Total electron exposure (e^-/Å)	50	50	
Frames collected during exposure (no.)	42	42	
Defocus range (μm)	- 0.8 ~ -2.2	- 0.8 ~ -2.2	
Automation software	EPU	EPU	
Micrographs collected (no.)	9,931	13,550	
Micrographs used (no.)	8,392	12,716	
Total extract particles (no.)	6,359,431	8,205,750	
For each reconstruction			
Refined particles (no.)	174,645	124,367	109,194
Final particles (no.)	174,645	124,367	109,194
Point group	C1	C1	C1
Resolution (global, Å)			
FSC=0.5/0.143	4.16/3.58	4.14/3.58	4.08/3.56
Map sharpening B factor ($Å^2$)	101.7	112.8	98.1
Map sharpening methods	DeepEMhancer	Half-maps correlation	Half-maps correlation
Model composition			
Protein	1081	1070	747
Ligands	2	2	4

Model refinement			
Refinement package	PHENIX	PHENIX	PHENIX
- real or reciprocal space	Real Space	Real Space	Real Space
- resolution cutoff	3.58	3.58	3.56
Model-Map scores			
- CC	0.64	0.73	0.82
B factors (Å^2)			
Protein residues	119.31	102.44	113.53
Ligands/DNA/RNA	20	136.56	30
R.m.s. deviations from ideal values			
Bonds length (Å)	0.005	0.005	0.005
Bond angles (°)	0.689	0.690	0.787
Validation			
MolProbity score	1.11	1.36	1.33
CaBLAM outliers	0.69	0.60	0.84
Clashscore	2.43	3.61	6.07
Poor rotamers (%)	0	0	0.30
C-beta deviations	0	0	0
EMRinger score	1.11	1.15	1.51
Ramachandran Plot			
Favored (%)	97.61	96.71	98.22
Outliers (%)	0	0	0

197